Improved Linear Active Disturbance Rejection Controller Control Considering Bus Voltage Filtering in Permanent Magnet Synchronous Generator

XUESONG ZHOU, MAO LIU[iD], YOUJIE MA, AND SUNA WEN

Tianjin Key Laboratory for Control Theory and Applications in Complicated Industry Systems, School of Electrical and Electronic Engineering, Tianjin University of Technology, Tianjin 300384, China

Corresponding author: Mao Liu (mao_tjlg@163.com)

ABSTRACT In the permanent magnet direct drive wind power generation system, the direct current (DC) bus voltage signal of the converter is usually used as the feedback of the voltage outer loop. Because of the existence of random white noise and the measurement error when the sensor collects the DC bus voltage signal, it is necessary to filter the bus voltage signal through the first-order inertial link. The time constant of the first order inertial link is usually 10ms-15ms. In the traditional voltage external loop second-order active disturbance rejection controller (ADRC) system, the influence of the bus voltage filter is not considered in the design of ADRC, which results in the phase lag and amplitude offset between the feedback of the controller and the real bus voltage. This will make the performance of the system affected by the time constant of the first-order inertial link. In this paper, an improved ADRC considering the bus voltage filter is proposed. The filtered bus voltage is expanded into a new state variable. The voltage before the filter is estimated by using the fourth-order linear expansion state observer (LESO) and used as the feedback. The simulation results show that the improved ADRC system has better control performance.

INDEX TERMS Permanent magnet synchronous generator, wind power generation, linear active disturbance rejection control, measurement noise, extended state observer.

I. INTRODUCTION

Wind power generation technology has achieved rapid development and wide application in recent years, in which variable speed constant frequency (VSCF) wind power technology has become a research hotspot in this field [1], [2]. VSCF wind power generation system mainly includes direct drive permanent magnet synchronous generator (PMSG) system [3], [4] and doubly fed wind power generation system [5], [6]. The former omits expensive and precise gear box, slip ring and other vulnerable parts. Moreover, the back-to-back full power converter, which has the characteristics of simple structure, small friction loss and high conversion efficiency, has gradually become the focus of research [7].

The associate editor coordinating the review of this manuscript and approving it for publication was Xiaodong Liang[iD].

In the full power converter, the double closed-loop structure of DC bus voltage outer loop and current inner loop is usually used to realize power conversion and stabilize bus voltage [8]. When the output power of the system and the disturbance and load change suddenly, the unbalance between the output of the grid-side converter and the output of the machine-side converter will occur, which will cause the DC-side bus voltage to rise, and then the converter will not work properly. When the external disturbance is large, the protective action will be triggered, which will eventually lead to the collapse of the system [9]. At present, the control problem of DC bus voltage is a research hotspot. In [10], an improved method of simultaneously suppressing the second harmonic (2h) dc-bus voltage pulsation and torque ripple by a compensation unit in parallel with the dc bus in the PMSG system with asymmetric impedance is proposed. Compared to the existing methods, the proposed method uses

fewer power devices and requires a much lower compensation current. In [11], the super-twisting algorithm predictive current control (STA-PCC) was applied to the voltage source converter (VSC) to regulate the DC bus voltage and current for the purpose of enhancing dynamic tracking behavior of the power and improving the quality of the energy of the hybrid renewable energy system (HRES). In [12], a moving average filter (MAF) was used to filter the DC-side voltage. In order to make MAF have the flexibility to choose the bandwidth, an auxiliary look-ahead filter is used. However, this method has low sensitivity and relatively consumes RAM resources. In actual operation, the bus voltage stability can be maintained by applying auxiliary network side converter, energy storage protection circuit and energy dissipation protection circuit on the DC bus side [13]. Therefore, maintaining bus voltage stability is an important part of ensuring the stable operation of the system, and its control link is required to have strong anti-disturbance performance and robustness. At present, the bus voltage control of converter mainly relies on the traditional proportional integration (PI) control, which can track the given value without static error [14], [15]. However, PI control mainly relies on the difference between the given value and the feedback signal for proportional integral operation, which causes the system to have a slow transient process. In addition, there is a contradiction between overshoot and rapidity. Therefore, K. Ohnishi, a Japanese scholar, first proposed Disturbance Observer (DOB), which can effectively improve the system's anti-disturbance performance by observing and compensating the disturbances to the system [16]. Disturbance compensation is to observe the total disturbance of the controlled object, including internal disturbance and external disturbance. Compensation through disturbance compensation can improve the robustness of the system. Among them, the ADRC proposed by Han provides a new idea for disturbance compensation method [17]–[19]. The extended state observer (ESO), the core element of ADRC, can accurately estimate the state variables in the controlled system. Moreover, the uncertain part of the model and the external force from the environment can be observed in real time. It can be expanded into a new state variable and compensated by the disturbance compensation link. The ADRC compensates the controlled system to the integrator series. Therefore, the active disturbance rejection control does not need to rely on an accurate mathematical model [20]–[23]. For practical systems whose control gain is difficult to determine, the state variables can also be accurately estimated. This method has been widely used in PMSG control [24].

In the digital control system, because of quantization error and other reasons, the measured noise will exist in the calculated DC bus voltage. Therefore, the DC voltage signal is usually filtered by the first-order inertia link and used as the feedback input of the controller. The scientific research work of filtering the measured signal includes: in [25], Kalman filter is proposed to filter the measured signal of the controlled system, so that the reduced-order extended state observer has higher observation accuracy, but the computation of this filtering algorithm is too large to affect its convergence speed. In [26], a robust differentiator based on super twisting algorithm is proposed, which can filter the input signal, and its convergence speed is more dependent on the selection of control parameters, and no parameter tuning rules are given. All of the above methods can effectively filter the measured signal, but the difference of amplitude and phase between the filtered signal and the actual system output is not considered, which affects the output of the controller and reduces the system performance. In the digital simulation, the filtering time constant of the first-order inertial link in the traditional PI control system is usually taken as 1ms. However, the filtered signal still contains interference signals with large frequency and amplitude, which results in large fluctuation range of the bus voltage controlled by the second-order LADRC. When the filtering time constant is increased to 10 ms, the high frequency noise content of the filtered signal is greatly reduced. However, there are differences in amplitude and phase between the filtered signal and the actual system output, resulting in low-frequency ripple of bus voltage. In ADRC theory, the scientific research work of filtering the measurement signal includes: In [27], an integral extended state observer (IESO) is proposed to deal with the measurement signal of doped noise, and an integral ADRC is constructed based on it. However, this method is prone to the phenomenon of integral saturation. In [28], digital filter and position tracking observer are used for signal processing, but it will affect the dynamic performance of the driving system. Therefore, an improved position tracking observer based on model prediction method is proposed. The control strategy of ADRC adopts ESO and nonlinear error feedback control law to estimate and compensate the total disturbance. However, the model prediction method of this system is only suitable for medium and short-term prediction, and it is difficult to adjust the parameters in ADRC control. In this paper, an improved ADRC with bus voltage filter is proposed for the first time, which expands the filtered bus voltage into a new state variable. The fourth-order linear expansion state observer is used to estimate the voltage value before filtering and use it as the feedback signal of LADRC, thereby eliminating the effect of the first-order inertia link on the system performance.

The influence of bus voltage filter structure is not considered in the traditional second-order linear ADRC control, which will result in the difference of amplitude and phase between the feedback signal and the real system output, thus affecting the output of the controller and reducing the system performance.

The rest of this paper is organized as follows. The modeling process of grid-side inverter is given in **Section II**. **Section III** introduces the traditional LADRC and bus voltage filtering links in detail. **Section IV** introduces the improved LADRC based on bus voltage filtering. **Section V**

shows digital simulations to verify the feasibility and effectiveness of the proposed improved LADRC control. Finally, several conclusions are summarized in **Section VI**.

II. MODELING OF GRID-SIDE INVERTERS
In direct-drive permanent magnet wind power generation system, the wind turbine converts the captured wind energy into rotational potential energy to drive the PMSG to work, and is connected to the power grid through a full-power converter. The grid-side converter mainly implements unit power factor operation and stabilizes the DC-side bus voltage. The machine side converter realizes the control of generator speed or torque. The wind energy conversion system has been illustrated in Fig. 1.
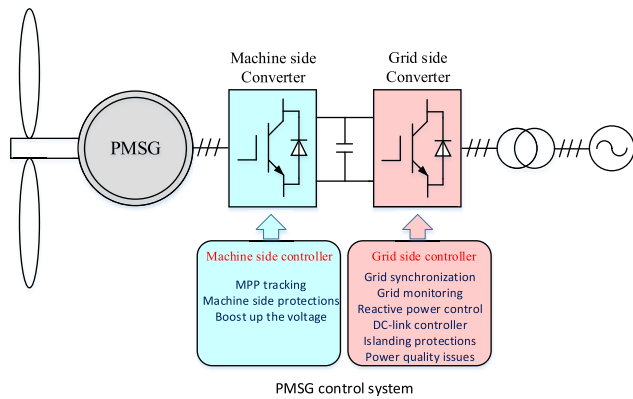
FIGURE 1. Schematic diagram of direct-drive permanent magnet synchronous generator.

Fig. 2 depicts the circuit equivalent model of the grid-side inverter. e_a, e_b and e_c represent the three-phase grid voltage. C, R and L are the bus filter capacitor, the resistor and the equivalent filter inductor, respectively. Where U_{dc} represents the DC side bus voltage and I_{dc} represents the current of the DC side capacitor. Where u_a, u_b and u_c denote grid-side inverter output phase voltage, while i_a, i_b and i_c depict three-phase grid current.
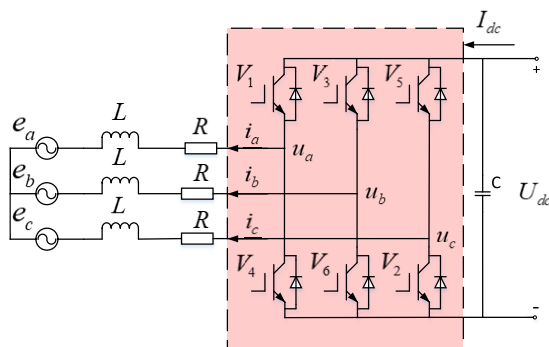
FIGURE 2. Main circuit topology diagram of grid side converter.

The state space expression of the grid-connected inverter established in the three-phase stationary coordinate

system is:

$$\begin{bmatrix} u_a \\ u_b \\ u_c \end{bmatrix} = \begin{bmatrix} e_a \\ e_b \\ e_c \end{bmatrix} + L \begin{bmatrix} \dfrac{di_a}{dt} \\ \dfrac{di_b}{dt} \\ \dfrac{di_c}{dt} \end{bmatrix} + R \begin{bmatrix} i_a \\ i_b \\ i_c \end{bmatrix} \quad (1)$$

The transformation matrix transformed from the three-phase stationary coordinate system ABC to the two-phase rotating coordinate system dq is:

$$C_{3s/2r} = \sqrt{\frac{2}{3}} \begin{bmatrix} \cos\theta & \cos(\theta - 2\pi/3) & \cos(\theta + 2\pi/3) \\ -\sin\theta & -\sin(\theta - 2\pi/3) & -\sin(\theta + 2\pi/3) \end{bmatrix} \quad (2)$$

Substituting the equation (2) into the equation (1), the state space expression of the control object in the two-phase rotating coordinate system is obtained:

$$\begin{bmatrix} u_d \\ u_q \end{bmatrix} = \begin{bmatrix} e_d \\ e_q \end{bmatrix} + L \begin{bmatrix} \dfrac{di_d}{dt} \\ \dfrac{di_q}{dt} \end{bmatrix} - \begin{bmatrix} 0 & -\omega L \\ \omega L & 0 \end{bmatrix} \begin{bmatrix} i_d \\ i_q \end{bmatrix}$$
$$+ R \begin{bmatrix} i_d \\ i_q \end{bmatrix} \quad (3)$$

where ω is the angular frequency of the dq synchronous rotating coordinate system. u_d, u_q denote component of the inverter output voltage on the dq axis of the rotating coordinate, e_d, e_q are the component of the grid voltage on the dq axis of the rotating coordinate, respectively, i_d and i_q represent component of the grid side current on the dq axis of the rotating coordinate, respectively.

The expressions of active power and reactive power output from grid-connected converter to power grid are as follows:

$$\begin{cases} P = e_d i_d + e_q i_q \\ Q = e_q i_d - e_d i_q \end{cases} \quad (4)$$

In which, P greater than zero indicates that the converter works in the inverted state, and the active power flows from the DC side to the alternating current (AC) network. P less than zero indicates that the converter works in the rectifier state, and the active power flows from the AC network to the DC side. Q greater than zero means that the converter emits lagged reactive power to the grid; Q less than zero means that the converter absorbs lagged reactive power from the grid.

Through the grid voltage vector orientation, $e_d = E$, $e_q = 0$. E is the peak value of the grid phase voltage. When the system reaches steady state, the differential term in equation (3) is zero and can be further reduced to equation (5). In equation (6), i_d and i_q describe the active and reactive components, respectively.

$$\begin{cases} u_d = e_d + Ri_d + \omega L i_q \\ u_q = Ri_q - \omega L i_d \end{cases} \quad (5)$$

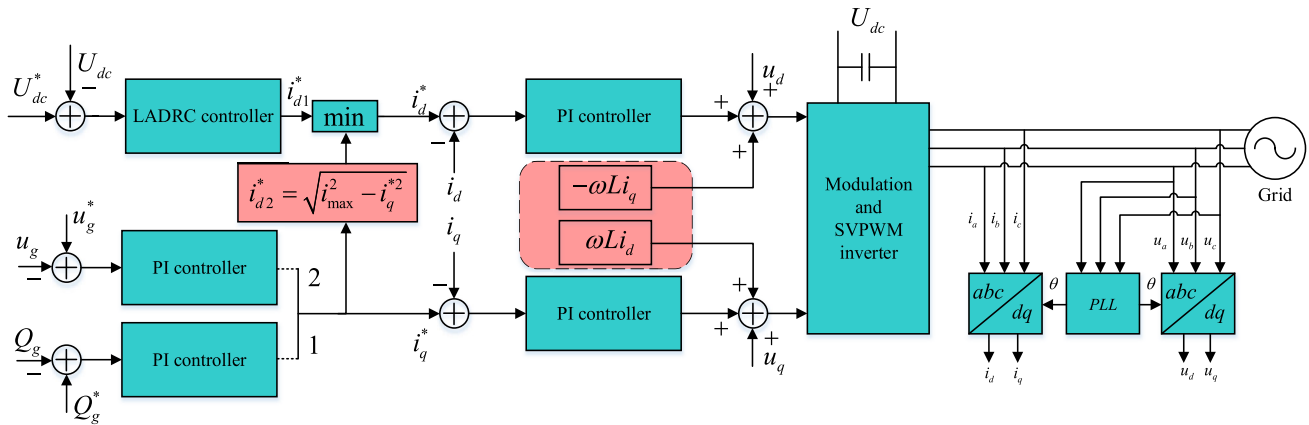$$\begin{cases} P = e_d i_d \\ Q = -e_d i_q \end{cases} \quad (6)$$

FIGURE 3. Control block diagram of grid-side inverters.

Equation (6) clearly shows that active and reactive power can be decoupled by coordinate transformation. D-axis current regulates active power and q-axis current controls reactive power. In the voltage outer loop, the given input of the LADRC controller is obtained by comparing the voltage target value of the DC bus U_{dc}^* with the voltage feedback value U_{dc}. The controller can output the given value i_{d1}^* of the d-axis of the inner current loop. The q-axis of the inner current loop can be divided into two operation modes. 1. Port 1 represents the unit power factor mode. 2. Port 2 represents STATCOM mode. When the system runs steadily, the inverters work in mode 1, and the wind turbines can be connected to the grid with unit power factor. When the system is disturbed and operates in the transient process, the inverters work in mode 2, which gives priority to reactive current. Therefore, the reactive power support of the converter to the grid voltage can be realized. Because of the limitation of the current amplitude of the converter, the output of the outer q-axis needs to be limited by $i_{d2}^* = \sqrt{i_{max}^2 - i_q^{*2}}$, so the reference value i_d^* of the inner q-axis current can be obtained. After comparing with the output of the outer d-axis current, the smaller value is taken as the given value of the active current. The control block diagram of the grid-side inverter is shown in Fig. 3.
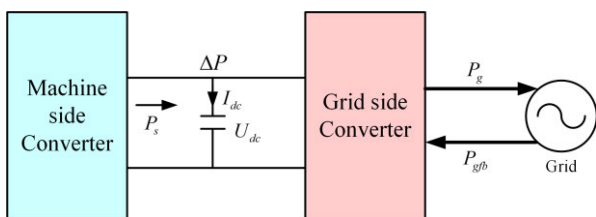

FIGURE 4. Schematic diagram of power balance.

Fig. 4 depicts the power balance relationship between PMSG and power grid. When the system is in steady state operation, $p_m = p_s = p_g$, the power injected into the grid and the power from the wind turbine are maintained

in equilibrium. Fluctuations in the grid voltage will affect the imbalance between the machine side and the grid side, $p_s \neq p_g$. When the grid voltage drops, the inverters increase the output current to ensure constant power output. Due to the current amplitude limit of the converter and the constant output of the machine side power, when the maximum current is reached, the inverter output power will decrease rapidly, resulting in the output power in the busbar being less than the input power. As a result, the energy on the DC side accumulates rapidly and the voltage rises. The bus voltage control equation is:

$$\Delta P = U_{dc}I_{dc} = P_s - P_g = \frac{1}{2}C\frac{dU_{dc}^2}{dt} \tag{7}$$

When the system is subjected to high voltage faults, the output active current will decrease due to the limitation of the converter capacity. The energy in the power grid will be poured back to the DC side, which will cause bus voltage to rise sharply beyond its endurance range, resulting in damage to power electronic devices. The power balance relationship of PMSG is as follows:

$$\Delta P = U_{dc}I_{dc} = P_s + P_{gfb} - P_g = \frac{1}{2}C\frac{dU_{dc}^2}{dt} \tag{8}$$

From the above analysis, it can be concluded that when the grid side fault occurs, the inverters are first impacted, while the generators are passively impacted by the grid side. Because the generator side and the grid side are coupled by DC capacitors, maintaining the voltage stability of the DC side bus is the key for wind power system to operate without disconnection when the grid side fails.

In this paper, an improved second-order LADRC is designed as the controller of d-axis outer loop. Compared with the traditional second-order LADRC, the improved LADRC eliminates the influence of amplitude change and phase lag caused by bus voltage filtering, and further improves the performance of the controller to ensure the stability of bus voltage on the DC side.

III. TRADITIONAL LADRC SYSTEM AND BUS VOLTAGE FILTERING

LADRC consists of linear state error feedback rate (LSEF), linear extended state observer (LESO) and linear tracking differentiator (LTD), as shown in Fig. 5. LTD is used to arrange the transition process, eliminate the contradiction between overshoot and rapidity, and extract differential signals. Due to the given value characteristic, Ltd is not used in this paper. In Fig. 5, v, y are the reference value of DC bus voltage and the output of system, respectively; b_0 represents the control gain; u is the control variable, and the physical meaning is the output voltage of inverters; z_1, z_2 and z_3 are the output of LESO observation system, its differential, and sum disturbance.
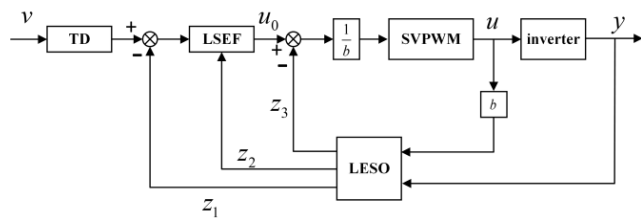

FIGURE 5. Traditional structure of LADRC.

A. MODEL OF CONTROLLED SYSTEM

The DC bus voltage U_{dc} is selected as the state variable x_1, the inverter voltage U_d as the control variable u, and the total disturbance is expanded to a new state variable x_3. The state equation of the system is as follows:

$$\begin{cases} \dot{x}_1 = x_2 \\ \dot{x}_2 = bu + x_3 \end{cases} \tag{9}$$

Define y_1 as the observation of state x_1. y_1 is the sum of the actual output of the system and the observed noise δ_n. The relationship between the above variables is $y_1 = x_1 + \delta_n$. To reduce noise, the bus voltage signal is typically filtered and used as a feedback input to the controller. The filter is now designed as the first-order inertia link of the cutoff frequency ω_t or the filter time constant T, and the filtered state quantity x_0 is obtained:

$$x_0(s) = \frac{1}{Ts+1} y_1(s) = \frac{\omega_t}{s+\omega_t} y_1(s) \tag{10}$$

where $T\omega_t = 1$, $T = 0$ indicates that the feedback signal is unfiltered.

The state equation and output equation of the converter system can be described as (11):

$$\begin{cases} \dot{x}_0 = -\omega_t x_0 + \omega_t y_1 \\ \dot{x}_1 = x_2 \\ \dot{x}_2 = bu + x_3 \end{cases} \tag{11}$$

B. PERFORMANCE COMPARISON OF DIFFERENT ORDER LADRC CONTROL DC BUS VOLTAGE

First-order to third-order LADRC controllers were tested in wind power systems [29]–[31]. TABLE 1 provides a comparison of the control performance of different orders of LADRC on wind power converter systems.

TABLE 1. Comparison of control performance of LADRC with different orders.

Performance index	First-order LADRC	Second-order LADRC	Third-order LADRC
Steady state error/V	Unstable	0	100
Rise time/s ($z_1 \rightarrow x_1$)	-	0.014	0.009
Total disturbance	-	2.09e7	Unstable
Voltage fluctuation range	-	±2.8%	-19.5% ~ 8.2%

The main performance indexes are: 1. Steady-state error; 2. Rise time (output of LESO tracking system); 3. Total disturbance; 4. Voltage fluctuation range of bus during voltage crossing.

TABLE 1 shows that the wind power converter system can achieve stability without steady-state error under the second-order LADRC control, and has strong tracking and anti-interference performance. The control effect of the first-order LADRC and the third-order LADRC is poor. In [32], it is proposed that the order of ADRC should be determined by the relative order of the system. Therefore, this paper designs a second order LADRC controller.

C. DESIGN OF THE FEEDBACK CONTROL LAW

Define the given value U_{dc}^* of bus voltage of inverters as v and the tracking error $e_s = v - x - 1$. The state equation of tracking error can be expressed as:

$$\ddot{e}_f = \ddot{v} - \ddot{x}_1 = \ddot{v} - bu - x_3 \tag{12}$$

The linear proportional differential feedback control law is used:

$$\ddot{e}_s = -k_d \dot{e}_s - k_p e_s \tag{13}$$

where k_p and k_d are the proportional gain of the controller and the differential gain of the controller, respectively.

The introduction of differential term in feedback control law makes use of the predictive property of differential, which can predict the trend of deviation. Therefore, it can produce advanced control effect and improve the dynamic performance of the system.

In the traditional PID control, the differential term can amplify the random noise and weaken the anti-interference performance of the system. However, LESO is essentially a

band-pass filter. By adjusting the parameters, the noise content of the output can be effectively reduced without affecting the performance of the system.

According to equation (12) and (13), the control output is:

$$u = \frac{\ddot{v} + k_d \dot{v} + k_p (v - x_1) - k_d x_2 - x_3}{b} \quad (14)$$

where $F(s) = (\ddot{v} + k_d \dot{v})$ is a differential feedforward term that eliminates the inherent error of the tracking input. The system output x_1, its differential x_2 and total disturbance x_3 cannot be directly obtained, and can be obtained by observer or sensor measurement.

D. LESO DESIGN WITHOUT CONSIDERING BUS VOLTAGE FILTERING

The third-order linear ESO is designed to observe the state of the system (3). The mathematical model is shown in equation (15), and its structural block diagram is presented in Fig. 6.

$$\begin{cases} e_1 = z_1 - x_0 \\ \dot{z}_1 = z_2 - \beta_1 e_1 \\ \dot{z}_2 = z_3 - \beta_2 e_1 + bu \\ \dot{z}_3 = -\beta_3 e_1 \end{cases} \quad (15)$$
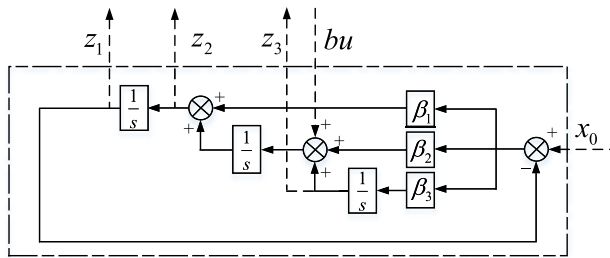

FIGURE 6. Third-order LESO block diagram.

In which, z_1, z_2 and z_3 are the estimated values of x_0, x_2 and total disturbance x_3, respectively. β_1, β_2, β_3 represent the observer error gains while e_1 is defined as the observation error of the LESO to the feedback x_0.

The transfer function of LESO obtained by equation (15) are given as follows:

$$\begin{cases} z_1 = \dfrac{(\beta_1 s^2 + \beta_2 s + \beta_3)x_0 + bus}{s^3 + \beta_1 s^2 + \beta_2 s + \beta_3} \\ z_2 = \dfrac{(\beta_2 s^2 + \beta_3 s)x_0 + (bs^2 + b\beta_1 s)u}{s^3 + \beta_1 s^2 + \beta_2 s + \beta_3} \\ z_3 = \dfrac{\beta_3 s^2 x_0 - b\beta_3 u}{s^3 + \beta_1 s^2 + \beta_2 s + \beta_3} \end{cases} \quad (16)$$

where $s^3 + \beta_1 s^2 + \beta_2 s + \beta_3$ is a characteristic polynomial of the third-order LESO. Through the pole placement method, $s^3 + \beta_1 s^2 + \beta_2 s + \beta_3$ can be configured into an ideal characteristic polynomial $(s + \omega_0)^3$, $\beta_1 = 3\omega_0$, $\beta_2 = 3\omega_0^2$, $\beta_3 = \omega_0^3$ and ω_0 be the observer bandwidth. By selecting the appropriate observer bandwidth, LESO can estimate system

state variables and total disturbances in real time, $z_1 \rightarrow x_1$, $z_2 \rightarrow x_2$, $z_3 \rightarrow x_3$.

Through equation (16), it is known that LESO has asymptotic convergence for step input. Replace x_1, x_2, x_3, in equation (14) with z_1, z_2 and z_3, to obtain theoretical control output u and actual control output u_1:

$$u = \frac{\ddot{v} + k_d \dot{v} + k_p (v - z_1) - k_d z_2 - z_3}{b} \quad (17)$$

$$u_1 = \begin{cases} u_{max}\,\mathrm{sgn}(u), & |u| > u_{max} \\ u, & |u| \le u_{max} \end{cases} \quad (18)$$

The second-order LADRC structure block diagram is illustrated in Fig. 7, and the second-order LADRC system control block diagram of bus voltage of inverters is depicted in Fig. 8.
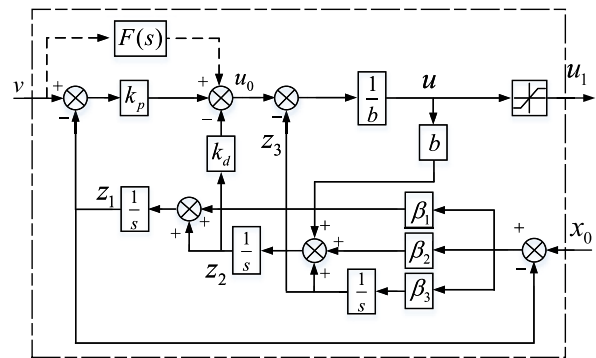

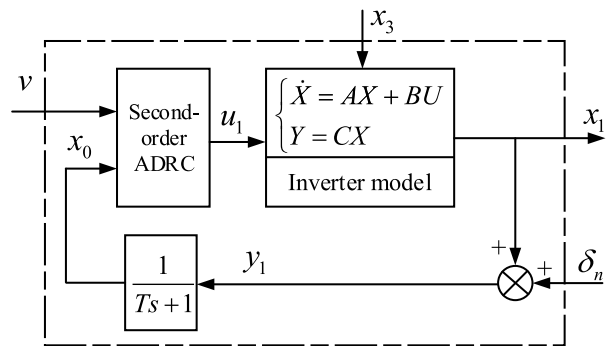**FIGURE 7. Second-order linear ADRC.**

FIGURE 8. Structural block diagram of ADRC system.

E. THE RELATIONSHIP BETWEEN SYSTEM PERFORMANCE AND FILTERING TIME CONSTANT

To simplify the analysis, the limiting of the control output is not considered in the following mathematical models. The equations (16) and (17) can be simplified as:

$$bu(s) = \frac{G_1}{G_3}v(s) - \frac{G_2}{G_3}x_0 \quad (19)$$

where

$$G_1(s) = (s^2 + k_d s + k_p)(s^3 + \beta_1 s^2 + \beta_2 s + \beta_3)$$
$$G_2(s) = (\beta_1 k_p + \beta_2 k_d + \beta_3)s^2 + (\beta_2 k_p + \beta_3 k_d)s + \beta_3 k_p$$
$$G_3(s) = [s^2 + (\beta_1 + k_d)s + \beta_1 k_d + \beta_2 + k_p]s \quad (20)$$

The output of the system can be obtained by equations (11) and (19):

$$x_1(s) = \frac{G_1 G_f v - G_2 \delta_n + G_3 G_f x_3}{G_f G_3 s^2 + G_2} \tag{21}$$

In which, $G_F(s) = Ts + 1$. $G_f G_3 s^2 + G_2$ is the system characteristic polynomial.

It can be known from equation (21) that the time constant of the filtering link in the feedback channel affects the anti-interference performance, tracking performance and noise suppression performance.

IV. IMPROVED ADRC CONSIDERING BUS VOLTAGE FILTERING

A. LESO CONSIDERING BUS VOLTAGE FILTERING

In order to eliminate the influence of the filtering process on the system performance, the fourth-order LESO is designed to observe the state of the system (5). The mathematical model is shown in equation (22), and its structural block diagram is depicted in Fig. 9.

$$\begin{cases} e_0 = z_0 - x_0 \\ \dot{z}_0 = -\omega_t z_0 + \omega_t (z_1 - \beta_0 e_0) \\ \dot{z}_1 = z_2 - \beta_1 e_0 \\ \dot{z}_2 = z_3 - \beta_2 e_0 + bu \\ \dot{z}_3 = -\beta_3 e_0 \end{cases} \tag{22}$$

where z_0, z_1, z_2 and z_3 are the estimated values of the state variables x_0, x_1, x_2 and the total disturbance x_2, respectively; e_0 is defined as the observation error of the fourth-order LESO to the feedback x_0; $\beta_0, \beta_1, \beta_2,$ and β_3 are the observer errors gains, respectively.
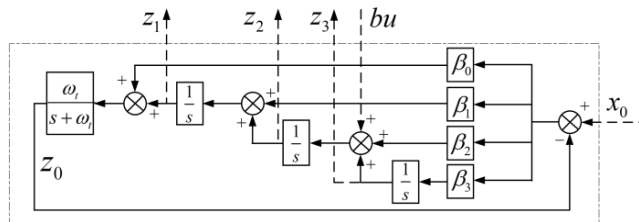

FIGURE 9. Fourth-order LESO structure block diagram.

Based on the equation (22), the transfer function of z_1, z_2, z_3 can be expressed as follows:

$$\begin{cases} z_1 = \frac{(\beta_1 s^2 + \beta_2 s + \beta_3)y_1 + (G_f + \beta_0)bus}{(G_f + \beta_0)s^3 + \beta_1 s^2 + \beta_2 s + \beta_3} \\ z_2 = \frac{(\beta_2 s^2 + \beta_3 s)y_1 + [(G_f + \beta_0)s^2 + \beta_1 s]bu}{(G_f + \beta_0)s^3 + \beta_1 s^2 + \beta_2 s + \beta_3} \\ z_3 = \frac{\beta_3(s^2 y_1 - bu)}{(G_f + \beta_0)s^3 + \beta_1 s^2 + \beta_2 s + \beta_3} \end{cases} \tag{23}$$

where $(G_f + \beta_0)s^3 + \beta_1 s^2 + \beta_2 s + \beta_3$ is a characteristic polynomial of the LESO. The equations (16) and (17) can be simplified as:

$$bu(s) = \frac{G_1}{G_3}v(s) - \frac{G_2}{G_3}y_1 \tag{24}$$

where

$$G_1(s) = (s^2 + k_d s + k_p)[(G_f + \beta_0)s^3 + \beta_1 s^2 + \beta_2 s + \beta_3]$$
$$G_2(s) = (\beta_1 k_p + \beta_2 k_d + \beta_3)s^2 + (\beta_2 k_p + \beta_3 k_d)s + \beta_3 k_p$$
$$G_3(s) = [(G_f + \beta_0)(s^2 + k_d s + k_p) + \beta_1(k_d + s) + \beta_2]s \tag{25}$$

The system output can be obtained from equations (11) and (24):

$$x_1(s) = v - \frac{G_2}{G_1}\delta_n + \frac{G_3}{G_1}x_3 \tag{26}$$

When $T \neq 0$, $(G_f + \beta_0)s^3 + \beta_1 s^2 + \beta_2 s + \beta_3$ can be configured as an ideal feature polynomial $T(s + \omega_0)^4$ and ω_0 is the observer bandwidth by the pole placement method. The parameters of LESO are configured as follows:

$$\beta_0 = 4\omega_0 T - 1, \beta_1 = 6\omega_0^2 T, \beta_2 = 4\omega_0^3 T, \beta_3 = T\omega_0^4 \tag{27}$$

Therefore, the equation (25) can be expressed as follows:

$$G_1(s) = T(s^2 + k_d s + k_p)(s^4 + 4\omega_0 s^3 + 6\omega_0^2 s^2 + 4\omega_0^3 s + \omega_0^4)$$
$$G_2(s) = T\omega_0^2[(\omega_0^2 + 4k_d\omega_0 + 6k_p)s^2$$
$$\qquad + (k_d\omega_0^2 + 4k_p\omega_0)s + \omega_0^2 k_p]$$
$$G_3(s) = T[s^4 + (4\omega_0 + k_d)s^3 + (6\omega_0^2 + 4k_d\omega_0 + k_p)s^2$$
$$\qquad + (4\omega_0^3 + 6k_d\omega_0^2 + 4k_p\omega_0)s] \tag{28}$$

When $T = 0$, $(G_f + \beta_0)s^3 + \beta_1 s^2 + \beta_2 s + \beta_3$ is the ideal polynomial $(s + \omega_0)^3$. Then we have $\beta_1 = 3\omega_0$, $\beta_2 = 3\omega_0^2$, $\beta_3 = \omega_0^3$.

It can be known from equation (26) that the time constant of the filtering link in the feedback channel does not affect the anti-interference performance, tracking performance and noise suppression performance.

B. CONVERGENCE ANALYSIS OF LESO

According to the formulas (23) and (27), the transfer functions of $z_1, z_2,$ and z_3 can be obtained:

$$z_1 = \frac{(6\omega_0^2 s^2 + 4\omega_0^3 s + \omega_0^4)y_1 + (s^2 + 4\omega_0 s)bu}{(s + \omega_0)^4}$$

$$z_2 = \frac{\omega_0^3(4s^2 + \omega_0 s)y_1 + (s^3 + 4\omega_0 s^2 + 6\omega_0^2 s)bu}{(s + \omega_0)^4}$$

$$z_3 = \frac{\omega_0^4(s^2 y_1 - bu)}{(s + \omega_0)^4} \tag{29}$$

Define the following tracking error: $e_1 = z_1 - y_1$, $e_2 = z_2 - \dot{y}_1$, $e_3 = z_3 - x_3$. Substituting equation (29) into the tracking error:

$$e_1 = \frac{s(4\omega_0 + s)(s^2 y_1 - bu)}{(s + \omega_0)^4}$$

$$e_2 = \frac{s(s^2 + 4\omega_0 s + 6\omega_0^2)(s^2 y_1 - bu)}{(s + \omega_0)^4} \tag{30}$$

According to equation (11), we can deduce that:

$$x_3 = \dot{x}_2 - bu = \ddot{y} - bu \tag{31}$$

The equation (31) is substituted for e_3:

$$e_3 = \frac{s(s^3 + 4\omega_0 s^2 + 6\omega_0^2 s + 4\omega_0^3)(s^2 y_1 - bu)}{(s + \omega_0)^4} \quad (32)$$

To make the analysis more typical, both y and u take the step signal with amplitude K, the steady-state error can be obtained as:

$$\begin{cases} e_{1s} = \lim_{s \to 0} se_1 = 0 \\ e_{2s} = \lim_{s \to 0} se_2 = 0 \\ e_{3s} = \lim_{s \to 0} se_3 = 0 \end{cases} \quad (33)$$

The improved LESO obtained from equation (33) can track the system output, the differential of the system output and total disturbance without steady-state error.

The following is a further analysis of the convergence characteristics of LESO in the time and frequency domain:

When the observer bandwidth is 50, 100, and 200, the improved LESO step response and frequency characteristics are shown in Figure 10 and Figure 11, respectively.
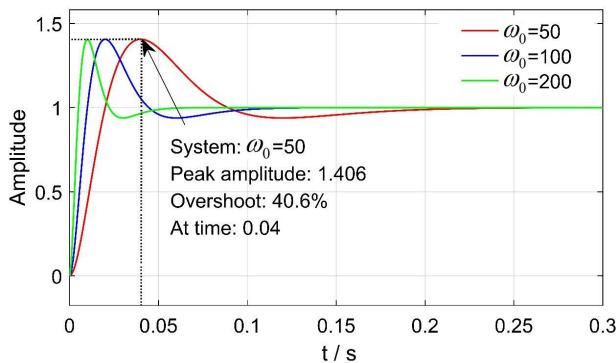

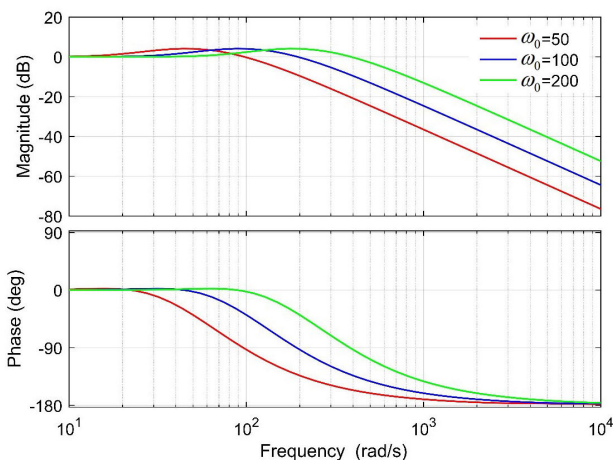**FIGURE 10.** Step response curve for improved LESO.

FIGURE 11. Frequency characteristics of improved LESO.

As can be seen from Figure 10, as the bandwidth of the observer increases, the response speed of the improved LESO

increases, and there is no static difference in the steady state. The amount of overshoot remains the same, about 40.6%. Therefore, it can be concluded that the observer bandwidth only affects the rapidity of the improved LESO response, and the overshoot is not affected by the bandwidth. Quantitative analysis is given below:

The response to step signal in equation (29) is as follows:

$$z_1(s) = \frac{6\omega_0^2 s^2 + 4\omega_0^3 s + \omega_0^4}{(s + \omega_0)^4} \frac{K}{s}$$
$$= K(\frac{1}{s} - \frac{1}{s + \omega_0}) + K(-\frac{\omega_0}{(s + \omega_0)^2}$$
$$+ \frac{5\omega_0^2}{(s + \omega_0)^3} - \frac{3\omega_0^3}{(s + \omega_0)^4}) \quad (34)$$

Laplace inverse transformation of equation (34) can be simplified:

$$z_1(t) = K - K(\frac{1}{2}\omega_0^3 t^3 - \frac{5}{2}\omega_0^2 t^2 + \omega_0 t + 1)e^{-\omega_0 t} \quad (35)$$

The derivative of equation (35) can get the extreme points as:

$$t_1 = 2/\omega_0, \quad t_2 = 6/\omega_0 \quad (36)$$

Substituting equation (36) into (35) can be solved:

$$\begin{cases} z_1(t_1) \approx 1.406K \\ z_1(t_2) \approx 0.938K \end{cases} \quad (37)$$

Obviously, the conclusion of Figure 10 can be verified by equation (37). From Figure 11, it can be found that with the increase of observer bandwidth, the frequency domain characteristic curve moves to the right, and the peak gain of equal amplitude occurs in the intermediate frequency segment. This feature is consistent with the conclusion of time domain analysis, that is, the overshoot is independent of bandwidth. The increase of high-frequency gain leads to the decrease of the system's ability to suppress high-frequency noise.

C. TRACKING PERFORMANCE ANALYSIS OF INPROVED SYSTEM

Depending on whether the input signal has first and second derivatives, the system given signal can be divided into continuously varying sinusoidal inputs and non-continuously varying step inputs.

When the sinusoidal signal is input to the controlled system, it is divided into cosine quantities, and the inherent error of the tracking input can be eliminated by the feedforward term. It can be known from equation (26) that the controlled system can be input without static tracking.

When the input of the system is a step signal, the derivative of the input is a pulse signal. In the actual system, the influence of this signal through feedforward is negligible. Therefore, the transfer function of the system given by input $v(s)$ can be expressed as:

$$\Phi(s) = \frac{k_p}{s^2 + k_d s + k_p} \quad (38)$$

It can be seen from equation (38) that the step response speed of the system depends on the proportional and differential amplification factors.

D. ANALYSIS OF ANTI-INTERFERENCE PERFORMANCE OF IMPROVED SYSTEM

The transfer function of the system under the action of disturbance $x_3(s)$ can be represented from equation (26):

$$\Phi_1(s) = \frac{x_1(s)}{x_3(s)} = \frac{G_3(s)}{G_1(s)} \tag{39}$$

When $\omega_0 = 50$, $k_p = 20$, $k_d = 10$ and T take 0 ms, 0.1 ms and 1 ms, respectively. Fig. 12 shows the frequency domain characteristic curve of the system (39). As can be seen from the Fig. 12, the time constant of the filtering link no longer affects the anti-interference performance of the system, but it is slightly worse than that without filtering.
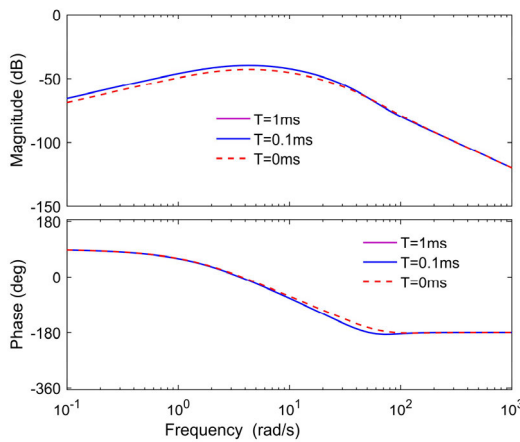
**FIGURE 12. Frequency domain characteristic curve of system anti-total disturbance.**

The influence of controller and observer parameters on disturbance rejection is discussed below. According to the pole configuration method, the parameters of the controller are configured as follows:

$$\begin{cases} k_p = \omega_c^2 \\ k_d = 2\omega_c \end{cases} \tag{40}$$

where ω_c is the controller bandwidth.

Substituting the equation (40) into (39) shows that the influence of the external disturbance x_3 on the system is mainly related to ω_c and ω_0. The parameters are assigned as follows: (1) $\omega_0 = 10$, $\omega_c = 10, 20...,50$. (2) $\omega_c = 10$, $\omega_0 = 10, 20...,50$. The Bode diagram of the system are shown in Fig. 13 and Fig. 14; From the above two figures, we can know that increasing ω_c and ω_0 can reduce the disturbance gain, thus enhancing the anti-interference performance of the system.

Assuming that the total disturbance x_3 is a unit step signal, the output response of the system is obtained according to
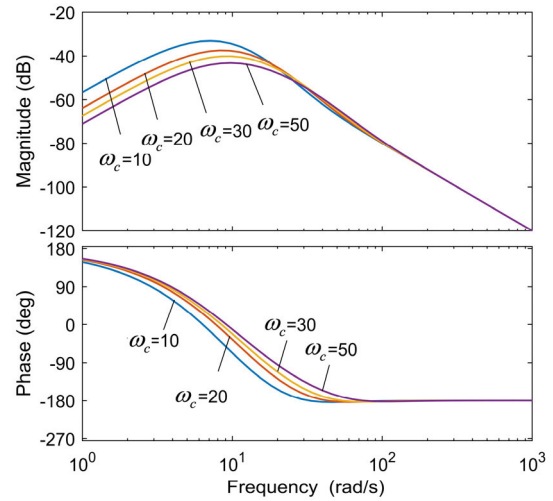
FIGURE 13. Bode diagram of total perturbation transfer function (When the controller bandwidth changes).
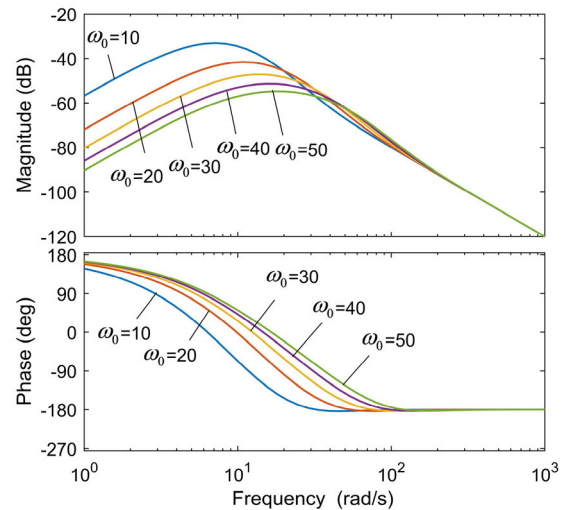
FIGURE 14. Bode diagram of total perturbation transfer function (When the observer bandwidth changes).

equation (39) and partial decomposition is performed:

$$x_1(s) = \frac{C_1(s)}{C_2(s)} = \frac{a_1}{(s+\omega_0)^4} + \frac{a_2}{(s+\omega_0)^3} + \frac{a_3}{(s+\omega_0)^2} + \frac{a_4}{s+\omega_0} + \frac{c_1}{(s+\omega_c)^2} + \frac{c_2}{s+\omega_c} \tag{41}$$

where

$$C_1(s) = s^3 + (4\omega_0 + 2\omega_c)s^2 + (6\omega_0^2 + 8\omega_c\omega_0 + \omega_c^2)s + 4\omega_0^3 + 12\omega_c\omega_0^2 + 4\omega_c^2\omega_0$$

$$C_2(s) = (s^2 + 2\omega_c s + \omega_c^2)(s^4 + 4\omega_0 s^3 + 6\omega_0^2 s^2 + 4\omega_0^3 s + \omega_0^4)$$

$$a_1 = \frac{\omega_0^3 + 6\omega_0^2\omega_c + 3\omega_0\omega_c^2}{(\omega_0 - \omega_c)^2}$$

$$a_2 = \frac{3\omega_0^3 + 15\omega_0^2\omega_c + 3\omega_0\omega_c^2 - \omega_c^3}{(\omega_0 - \omega_c)^3}$$

$$a_3 = \frac{6\omega_0^2(\omega_0 + 4\omega_c)}{(\omega_0 - \omega_c)^4} \quad a_4 = \frac{10\omega_0^2(\omega_0 + 3\omega_c)}{(\omega_0 - \omega_c)^5}$$

$$c_1 = \frac{2\omega_0^2(2\omega_0 + 3\omega_c)}{(\omega_0 - \omega_c)^4} \quad c_2 = \frac{-10\omega_0^2(\omega_0 + 3\omega_c)}{(\omega_0 - \omega_c)^5} \quad (42)$$

The inverse Laplace transformation of equation (42) is simplified to obtain:

$$x_1(t) = (\frac{1}{6}a_1t^3 + \frac{1}{2}a_2t^2 + a_3t + a_4)e^{-\omega_0 t} + (c_1t + c_2)e^{-\omega_c t}$$

(43)

When the system is stable:

$$\lim_{t \to \infty} x_1(t) = 0 \qquad (44)$$

Equation (44) can be understood as the steady state output response of the step disturbance is zero.

Equation (43) shows that the improved LADRC has better suppression performance for external disturbances and as the controller bandwidth ω_c and the observer bandwidth ω_0 increase, the decay speed of $x_1(t)$ is faster. Therefore, the adjustment time of the controlled system is shorter.

When $\omega_c = 20, 30, 50$, the suppression waveform of the closed-loop system to the step disturbance can be obtained, as shown in Fig. 15.
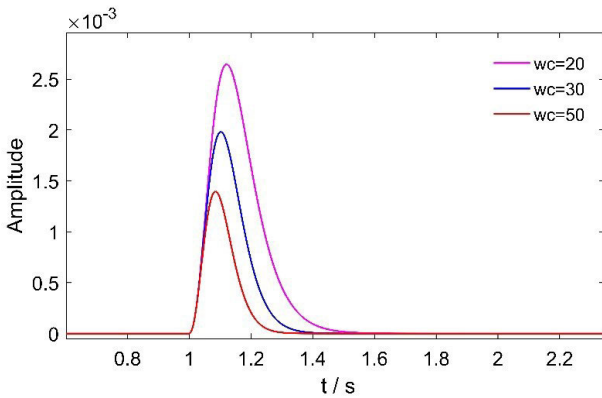

FIGURE 15. The comparison of different controller bandwidth to restrain step disturbance.

Both equation (43) and Fig. 15 show that the improved LADRC closed-loop system has strong capability of restraining external disturbance.

E. PERFORMANCE ANALYSIS OF THE IMPROVED SYSTEM FOR SUPPRESSING MEASUREMENT NOISE

From equation (26), the transfer function of the feedback channel to the control output is obtained by equation (45), and the transfer function of the observed noise to the system output is expressed by equation (46):

$$\frac{|bu(s)|}{\delta_n(s)} = \frac{G_2(s)}{G_3(s)} \qquad (45)$$

$$\frac{x_1(s)}{\delta_n(s)} = \frac{G_2(s)}{G_1(s)} \qquad (46)$$

The parameters are assigned as follows: $\omega_0 = 50, k_p = 20, k_d = 10, T = 0, 0.1, 1$. Fig.16 shows the frequency domain characteristic curves of equations (45) and (46). As can be seen from the figures, the improved system has the same suppression measurement noise performance when $T = 0.1$ ms and $T = 1$ ms. In addition, it was significantly improved compared with $T = 0$ ms.
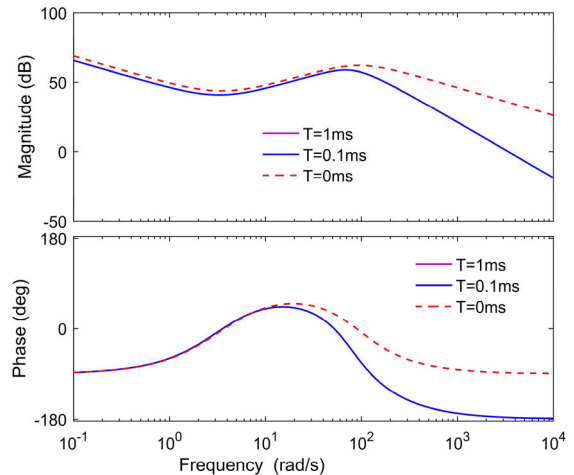
(a) Frequency domain characteristics of measuring noise to control
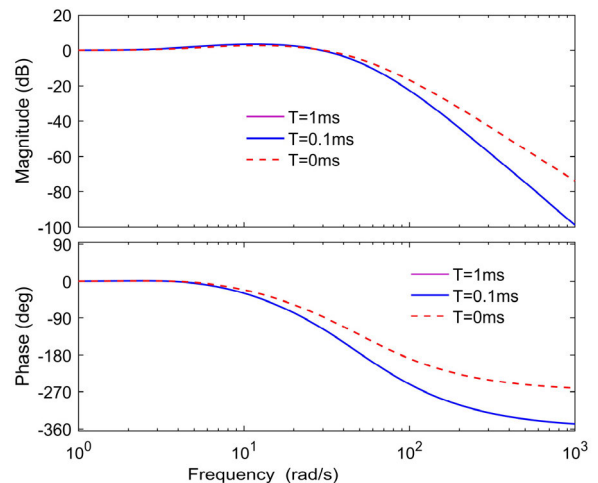
(b) Frequency domain characteristics of measuring noise to measuring noise

FIGURE 16. Bode diagram of total perturbation transfer function (When the observer bandwidth changes).

From the above simulation, it can be concluded that the inertia time constant does not affect the performance of the improved system when there is a filter link in the feedback channel. Moreover, compared with the bus voltage without filter, the anti-disturbance performance of the improved system decreases slightly, but the performance of suppressing the observation noise in the feedback channel is better. Since the improved system has strong filtering performance, the bandwidth of the improved LESO can be appropriately increased. Although some noise suppression performance is sacrificed, strong anti-interference performance can be obtained.

F. STABILITY ANALYSIS OF ACTUAL SYSTEMS

The structure of the LADRC system is shown in Fig.17, without considering the observational disturbance.
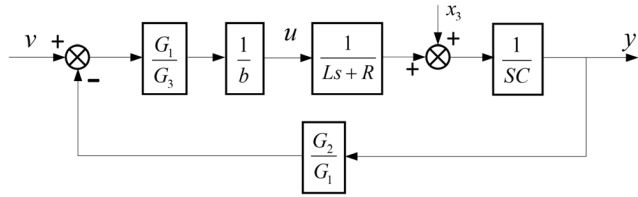
FIGURE 17. LADRC block diagram combined with the actual system.

According to Fig.17, the transfer function of the DC side bus voltage is established as follows:

$$x_1 = \frac{G_1}{LCb_0G_3s^2 + RCb_0G_3s + G_2}v$$
$$+ \frac{G_3b_0(Ls + R)}{LCb_0G_3s^2 + RCb_0G_3s + G_2}x_3$$
$$= G_vv + G_wx_3 \qquad (47)$$

where x_1, v and x_3 represent the DC side bus voltage, the bus voltage reference value and the external total disturbance; G_v is the transfer function of v to x_1; G_w is the transfer function of x_3 to x_1, which characterizes the anti-disturbance performance of the inverter.

The closed-loop transfer function of the reference input to the DC side bus voltage is obtained by equation (47):

$$x_1 = \frac{G_1/T}{a_6s^6 + a_5s^5 + a_4s^4 + a_3s^3 + a_2s^2 + a_1s + a_0}v \quad (48)$$

The coefficients are given in the Appendix A. From the expression, $a_i > 0$, $i = 0, 1, 2, 3, 4, 5, 6$.

According to the Lienard Chipart stability criterion, the necessary and sufficient condition for the stability of the system is that the odd Hurwitz determinant is positive:

$$\begin{cases} \Delta_3 > 0 \\ \Delta_5 > 0 \end{cases} \qquad (49)$$

where

$$\Delta_3 = \begin{vmatrix} a_5 & a_6 & 0 \\ a_3 & a_4 & a_5 \\ a_1 & a_2 & a_3 \end{vmatrix}$$

$$\Delta_5 = \begin{vmatrix} a_5 & a_6 & 0 & 0 & 0 \\ a_3 & a_4 & a_5 & a_6 & 0 \\ a_1 & a_2 & a_3 & a_4 & a_5 \\ 0 & a_0 & a_1 & a_2 & a_3 \\ 0 & 0 & 0 & a_0 & a_1 \end{vmatrix} \qquad (50)$$

Numerical calculations show that the improved LADRC system remains stable with wide variations in controller bandwidth ω_c and observer bandwidth ω_0. The change in bandwidth essentially changes the "time scale" of the system and does not affect the stability of the system within a certain range.

V. SIMULATION ANALYSIS

In order to verify the effectiveness of the improved linear auto-disturbance controller, a 1.5MW direct-drive permanent magnet synchronous generator model was built in Simulink. The grid-connected inverter control strategy is a DC voltage outer loop and a current inner loop double closed loop structure based on grid voltage vector orientation. A new linear active disturbance rejection controller based on discrete time is designed. The sampling time of the Simulink system is set to 1×10^{-6}s. The parameters of the controller and PMSG are listed in TABLE 2 and 3.

A. THE FUNCTION, EFFECT AND ELIMINATION METHOD OF FILTERING LINK

Fig.18 (a) describes the DC bus voltage waveforms when the inertia time constants T of the filter in the feedback channel of the controlled system are 0 ms and 4 ms, respectively. The bus voltage fluctuation ranges of the traditional system and the system with filter link are + 4.76% and + 1.12% respectively. It can be seen that the bus voltage fluctuation range of the traditional system is large, which shows that adding filter link in the feedback channel can improve the steady-state performance of the system. Fig.18 (b) shows the DC bus voltage waveform when the inertia time constant T are 0 ms and 15 ms respectively. By comparing the two curves, it can be seen that with the increase of the inertia time constant, the amplitude and phase difference between the feedback signal
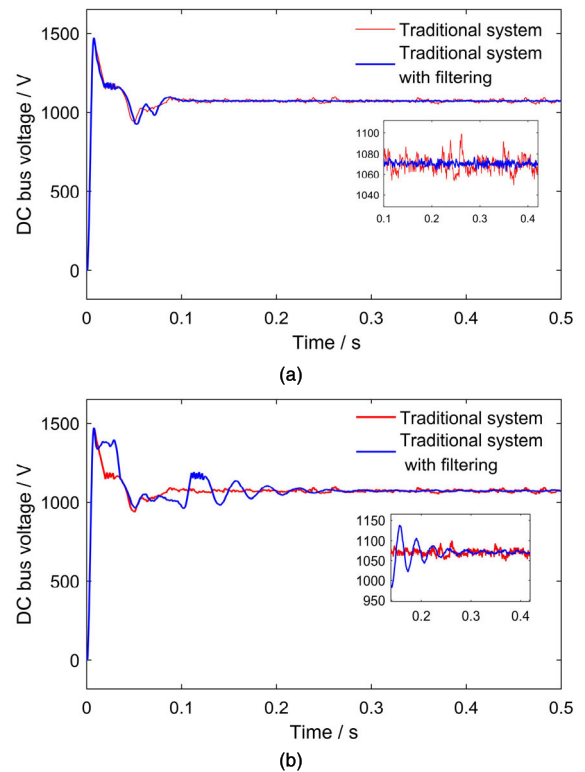
FIGURE 18. LADRC block diagram combined with the actual system.

and the actual system output will be caused, which will lead to the oscillation and instability of the system.

In order to eliminate the effect of increasing the filtering time constant on the steady-state performance of the system, an improved LADRC controller is used. Fig.19 is a comparison of bus voltage waveforms between the traditional system and the improved system when the filtering time constant T is 8ms. From the figure, we can know that the voltage value before filtering is observed by the fourth-order LESO as feedback, which eliminates the bus voltage oscillation caused by the filtering link and enhances the steady-state performance of the system.
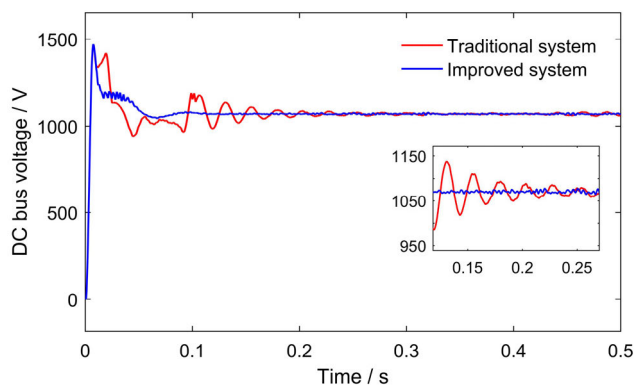

FIGURE 19. Comparison of bus voltage waveform between traditional system and improved system.

B. ANALYSIS OF DISTURBANCE REJECTION OF IMPROVED SYSTEM

In order to verify the anti-disturbance performance of the improved system, the bus voltage under disturbance is simulated by taking three-phase symmetrical fault of power grid as an example.

(i) The grid-connected point voltage symmetrically drops to 0.85p.u. at t = 0.3 and is cleared at t = 0.5s.

(ii) The grid-connected point voltage symmetrically rises to 1.1p.u. at t = 0.3 and is cleared at t = 0.5s.

Scenario 1

Fig.20(a) is a fault in which the three-phase voltage symmetrically drops to 0.85p.u. at t = 0.3s and recovers at t = 0.5s. In Fig.20, (b) and (c) are the simulation comparisons of the bus voltage between the traditional system and the improved system in the case of low voltage traversal. The observer bandwidth of LADRC in the improved system are 400 and 500, respectively. The observer bandwidth of LADRC in the traditional system is 400. As can be seen from Fig.20(b), the disturbance immunity of the improved system is slightly worse in the dynamic process of voltage drop and recovery at the grid-connected point, which verifies the theoretical analysis of Fig.12. In Fig.20(c), the observer bandwidth is increased to improve the anti-disturbance performance of the system.

Scenario 2

Fig.21(a) is a fault in which the three-phase voltage symmetrically rises to 0.85p.u. at t = 0.3s and recovers at t = 0.5s.
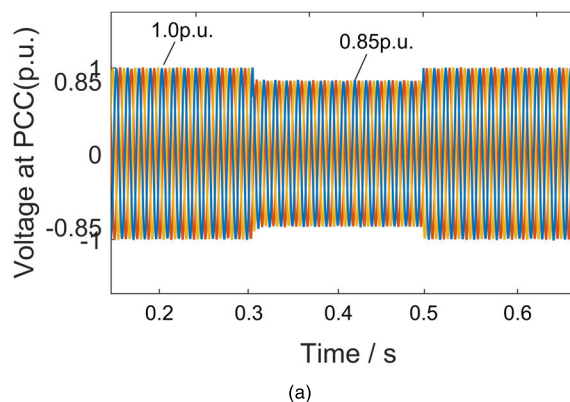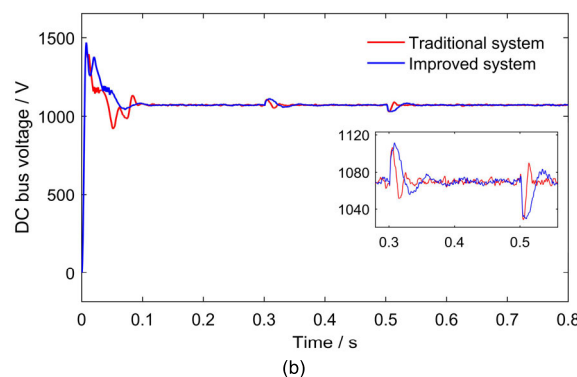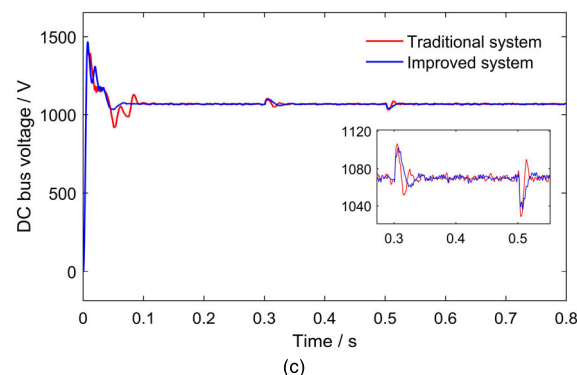
FIGURE 20. Comparison of system immunity under low voltage crossing.

The (b) and (c) in Fig.21 are the simulation comparisons between the traditional system and the improved system when high voltage traverse occurs. The observer bandwidth of LADRC in the improved system are 400 and 500 respectively. The observer bandwidth of LADRC in the traditional system is 400. As can be seen from Fig.21(b), the disturbance immunity of the improved system is slightly worse in the dynamic process of voltage drop and recovery at the grid-connected point, which also verifies the theoretical analysis of Fig.12. In Fig.21(c), the observer bandwidth is increased to improve the anti-disturbance performance of the system.

Through the above simulation experiments, it is shown that when the LESO observation bandwidth is constant, the anti-interference performance of the traditional system is slightly better than that of the improved system, but the performance of the improved system to suppress the measurement
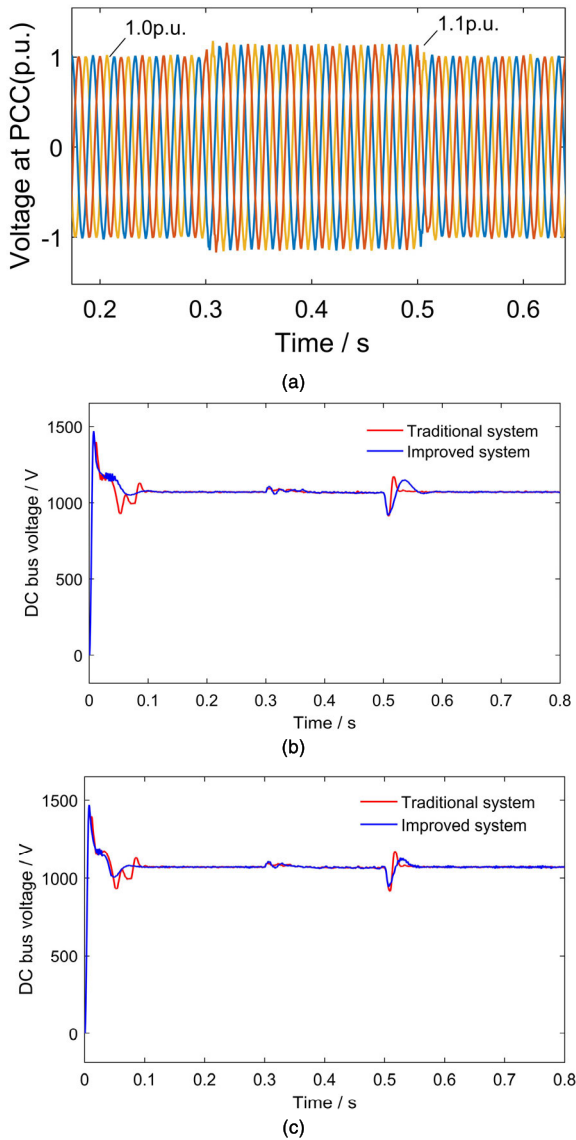
FIGURE 21. Comparison of system immunity during high voltage traversing.

noise is obviously improved. Therefore, the LESO bandwidth can be increased appropriately, and the noise suppression performance can be reduced partially to obtain stronger anti-interference performance. However, continuing to increase the bandwidth of the observer tends to cause the amplitude and frequency of the given value of the active current in the current inner loop to be large, thereby introducing 3rd and 5th harmonics into the grid current.

The above conditions are the simulation results under the standard model. Considering the actual operation state, the simulation under a reasonable model is carried out, and the above experimental results can be obtained. Reasonable model configuration: sampling deviation of DC bus is 1% of rated value, bus capacitance is 90% of standard value and filter reactance is 110% of standard value.

VI. CONCLUSION

In this paper, the filtered bus voltage is expanded into a new state variable in LESO, and the improved ADRC controller structure is applied to the grid connected inverter. The performance difference between traditional LADRC and improved LADRC in eliminating voltage ripple of DC bus is compared by simulation. In addition, when the LESO bandwidth is fixed, the anti-interference performance of the traditional system is slightly better than that of the improved system, but the performance of the improved system to suppress the measurement noise is significantly improved. Therefore, the bandwidth of LESO can be appropriately increased and the noise suppression performance can be reduced to obtain strong anti-interference performance. In addition, the digital simulation results show that the improved LADRC control system has strong anti-interference performance under the condition of voltage crossing at the grid side.

APPENDIXES
APPENDIX A

The expressions of $G_1(s)$, $G_2(s)$, and $G_3(s)$ in equation (28) are as follows:

$$G_1(s) = k_1 s^6 + k_2 s^5 + k_3 s^4 + k_4 s^3 + k_5 s^2 + k_6 s + k_7$$
$$G_2(s) = h_1 s^2 + h_2 s + h_3$$
$$G_3(s) = n_1 s^4 + n_2 s^3 + n_3 s^2 + n_4 s$$

where

$$k_1 = 1, k_2 = 4\omega_0 + 2\omega_c, \quad k_3 = 6\omega_0^2 + 8\omega_0\omega_c + \omega_c^2$$
$$k_4 = 4\omega_0^3 + 12\omega_0^2\omega_c + \omega_0\omega_c^2, \quad k_5 = \omega_0^4 + 8\omega_0^3\omega_c + 6\omega_0^2\omega_c^2$$
$$k_6 = 2\omega_0^4\omega_c + 4\omega_0^3\omega_c^2, \quad k_7 = \omega_0^4\omega_c^2$$
$$h_1 = \omega_0^4 + 8\omega_c\omega_0^3 + 6\omega_c^2\omega_0^2$$
$$h_2 = 2\omega_c\omega_0^4 + 4\omega_c^2\omega_0^3$$
$$h_3 = \omega_0^4\omega_c^2$$
$$n_1 = 1, \quad n_2 = 4\omega_0 + 2\omega_c$$
$$n_3 = 6\omega_0^2 + 8\omega_0\omega_c + \omega_c^2$$
$$n_4 = 4\omega_0^3 + 12\omega_c\omega_0^2 + 4\omega_c^2\omega_0$$

The expressions of a_0, a_1, a_2, a_3, a_4, a_5 and a_6 in equation (48) are as follows:

$$a_0 = h_3, \quad a_1 = h_2$$
$$a_2 = h_1 + RCbn_4$$
$$a_3 = LCbn_4 + RCbn_3$$
$$a_4 = LCbn_3 + RCbn_2$$
$$a_5 = LCbn_3 + RCbn_1$$
$$a_6 = LCbn_1$$

APPENDIX B
See Table 2.

APPENDIX C
See Table 3.

TABLE 2. Controller parameters.

Symbol	Quantity	Value
ω_c	Controller Bandwidth	2500
ω_0	Observer Bandwidth	700
b_0	Control gain	12000

TABLE 3. Parameters of direct-driven permanent magnet wind power inverter.

Symbol	Quantity	Value	Unit
P	Base power	1.5	MW
V_g	Base voltage	690	V
f	Base frequency	50	Hz
P_g	Rated generator	1	pu
n_p	Pole pairs of PMSG	12	
R_s	Stator phase resistance	0.0009	Ω
ϕ	Flux linkage	1.49	V.s
L_d, L_q	Stator inductance	0.573,0.874	mH
R_{ls}	Machine-side filter resistance	0.0002	Ω
C	DC capacitance	0.024	F
u_{dc}	DC link voltage	1070	V
R_g	Grid-side filter resistance	0.0009	Ω
L_g	Grid-side filter inductance	0.12	mH

REFERENCES

[1] F. M. Alhuwaishel, A. S. Morsy, and P. N. Enjeti, "A new active output filter (AOF) for variable speed constant frequency (VSCF) power system in aerospace applications," *IEEE Trans. Power Electron.*, vol. 33, no. 2, pp. 1087–1093, Feb. 2018.

[2] Y. Liu, S. Niu, and W. Fu, "Design of an electrical continuously variable transmission based wind energy conversion system," *IEEE Trans. Ind. Electron.*, vol. 63, no. 11, pp. 6745–6755, Nov. 2016.

[3] T. D. M. Bazzo, J. F. Kolzer, R. Carlson, F. Wurtz, and L. Gerbaud, "Multiphysics design optimization of a permanent magnet synchronous generator," *IEEE Trans. Ind. Electron.*, vol. 64, no. 12, pp. 9815–9823, Dec. 2017.

[4] J.-S. Lee, K.-B. Lee, and F. Blaabjerg, "Predictive control with discrete space-vector modulation of vienna rectifier for driving PMSG of wind turbine systems," *IEEE Trans. Power Electron.*, vol. 34, no. 12, pp. 12368–12383, Dec. 2019.

[5] W. Xu, K. Yu, Y. Liu, and J. Gao, "Improved coordinated control of standalone brushless doubly fed induction generator supplying nonlinear loads," *IEEE Trans. Ind. Electron.*, vol. 66, no. 11, pp. 8382–8393, Nov. 2019.

[6] M. E. Zarei, C. V. Nicolas, J. R. Arribas, and D. Ramirez, "Four-switch three-phase operation of grid-side converter of doubly fed induction generator with three vectors predictive direct power control strategy," *IEEE Trans. Ind. Electron.*, vol. 66, no. 10, pp. 7741–7752, Oct. 2019.

[7] A. Rodriguez-Cabero, M. Prodanovic, and J. Roldan-Perez, "Full-state feedback control of back-to-back converters based on differential and common power concepts," *IEEE Trans. Ind. Electron.*, vol. 66, no. 11, pp. 9045–9055, Nov. 2019.

[8] A. Mutovkin, V. Yuhimenko, M. Mellincovsky, S. Schacham, and A. Kuperman, "Control of direct voltage regulated active DC-link capacitance reduction circuits to allow plug-and-play operation," *IEEE Trans. Ind. Electron.*, vol. 66, no. 8, pp. 6527–6537, Aug. 2019.

[9] X. Zhang, P. Wei, W. Deng, S. Fan, X. Liu, and K. Li, "Control strategy of three-phase parallel PWM rectifier under unbalanced gird voltage," Tech. Rep., 2018.

[10] Y. Hu, Z. Q. Zhu, and M. Odavic, "An improved method of DC bus voltage pulsation suppression for asymmetric wind power PMSG systems with a compensation unit in parallel," *IEEE Trans. Energy Convers.*, vol. 32, no. 3, pp. 1231–1239, Sep. 2017.

[11] R. Benadli, B. Khiari, and A. Sellami, "Improving grid connected hybrid generation system using an adaptive super-twisting sliding mode and predictive current control strategy," *Control Eng. Appl. Inform.*, vol. 21, no. 2, pp. 64–75, 2019.

[12] R. Pena-Alzola, D. Campos-Gaona, P. F. Ksiazek, and M. Ordonez, "DC-Link Control filtering options for torque ripple reduction in Low-power wind turbines," *IEEE Trans. Power Electron.*, vol. 32, no. 6, pp. 4812–4826, Jun. 2017.

[13] Y. Huang, X. Yuan, J. Hu, P. Zhou, and D. Wang, "DC-bus voltage control stability affected by AC-bus voltage control in VSCs connected to weak AC grids," *IEEE J. Emerg. Sel. Topics Power Electron.*, vol. 4, no. 2, pp. 445–458, Jun. 2016.

[14] Y. Kanthaphayao and V. Chunkag, "Current-sharing bus and fuzzy gain scheduling of proportional–integral controller to control a parallel-connected AC/DC converter," *IET Power Electron.*, vol. 7, no. 10, pp. 2525–2532, Oct. 2014.

[15] A. Krama, L. Zellouma, A. Benaissa, B. Rabhi, M. Bouzidi, and M. F. Benkhoris, "Design and experimental investigation of predictive direct power control of three-phase shunt active filter with space vector modulation using anti-windup PI controller optimized by PSO," *Arabian J. Sci. Eng.*, vol. 44, no. 8, pp. 6741–6755, Aug. 2019.

[16] J. Yang, S. Li, and X. Yu, "Sliding-mode control for systems with mismatched uncertainties via a disturbance observer," *IEEE Trans. Ind. Electron.*, vol. 60, no. 1, pp. 160–169, Jan. 2013.

[17] J. Han, "From PID to active disturbance rejection control," *IEEE Trans. Ind. Electron.*, vol. 56, no. 3, pp. 900–906, Mar. 2009.

[18] H. Sira-Ramirez, J. Linares-Flores, C. Garcia-Rodriguez, and M. A. Contreras-Ordaz, "On the control of the permanent magnet synchronous motor: An active disturbance rejection control approach," *IEEE Trans. Control Syst. Technol.*, vol. 22, no. 5, pp. 2056–2063, Sep. 2014.

[19] Y. Su, C. Zheng, and B. Duan, "Automatic disturbances rejection controller for precise motion control of permanent-magnet synchronous motors," *IEEE Trans. Ind. Electron.*, vol. 52, no. 3, pp. 814–823, Jun. 2005.

[20] Y. Huang and W. Xue, "Active disturbance rejection control: Methodology and theoretical analysis," *ISA Trans.*, vol. 53, no. 4, pp. 963–976, Jul. 2014.

[21] H. Liu and S. Li, "Speed control for PMSM servo system using predictive functional control and extended state observer," *IEEE Trans. Ind. Electron.*, vol. 59, no. 2, pp. 1171–1183, Feb. 2012.

[22] J. Liu, S. Vazquez, L. Wu, A. Marquez, H. Gao, and L. G. Franquelo, "Extended state observer-based sliding-mode control for three-phase power converters," *IEEE Trans. Ind. Electron.*, vol. 64, no. 1, pp. 22–31, Jan. 2017.

[23] J. Yao and W. Deng, "Active disturbance rejection adaptive control of uncertain nonlinear systems: Theory and application," *Nonlinear Dyn.*, vol. 89, no. 3, pp. 1611–1624, Aug. 2017.

[24] Q. Shi, G. Wang, Y. Chen, L. Fu, W. Jiang, and H. Huang, "Frequency response control of D-PMSG based on the active disturbance rejection controller," in *Proc. 17th Int. Conf. Electr. Mach. Syst. (ICEMS)*, Oct. 2014, pp. 1379–1384.

[25] A. M. Boker and H. K. Khalil, "Nonlinear observers comprising high-gain observers and extended Kalman filters," *Automatica*, vol. 49, no. 12, pp. 3583–3590, Dec. 2013.

[26] S. Chen, X. Zhang, X. Wu, G. Tan, and X. Chen, "Sensorless control for IPMSM based on adaptive super-twisting sliding-mode observer and improved phase-locked loop," *Energies*, vol. 12, no. 7, p. 1225, Mar. 2019.

[27] J. Song, L. Wang, G. Cai, and X. Qi, "Nonlinear fractional order proportion-integral-derivative active disturbance rejection control method design for hypersonic vehicle attitude control," *Acta Astronautica*, vol. 111, pp. 160–169, Jun. 2015.

[28] G. Zhang, G. Wang, B. Yuan, R. Liu, and D. Xu, "Active disturbance rejection control strategy for signal injection-based sensorless IPMSM drives," *IEEE Trans. Transport. Electrific.*, vol. 4, no. 1, pp. 330–339, Mar. 2018.

[29] F. Alonge, M. Cirrincione, F. D'Ippolito, M. Pucci, and A. Sferlazza, "Active disturbance rejection control of linear induction motor," *IEEE Trans. Ind. Appl.*, vol. 53, no. 5, pp. 4460–4471, Sep. 2017.

[30] B.-Z. Guo and Z.-L. Zhao, "On convergence of the nonlinear active disturbance rejection control for MIMO systems," *SIAM J. Control Optim.*, vol. 51, no. 2, pp. 1727–1757, Jan. 2013.

[31] G. Wang, R. Liu, N. Zhao, D. Ding, and D. Xu, "Enhanced linear ADRC strategy for HF pulse voltage signal injection-based sensorless IPMSM drives," *IEEE Trans. Power Electron.*, vol. 34, no. 1, pp. 514–525, Jan. 2019.

[32] C. Zhao and D. Li, "Control design for the SISO system with the unknown order and the unknown relative degree," *ISA Trans.*, vol. 53, no. 4, pp. 858–872, Jul. 2014.

XUESONG ZHOU received the bachelor's degree in electrical engineering from the South China University of Technology, Guangzhou, China, in 1984, and the master's and Ph.D. degrees in electrical engineering from Tsinghua University, in 1990 and 1993, respectively.
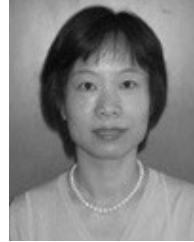
From 1993 to 2002, he was the Deputy Dean of the School of Electrical and Automation Engineering, Qingdao University. He joined the Tianjin University of Technology, as a Professor, in 2002. His research interests include the development and use of power electronics and renewable energy.
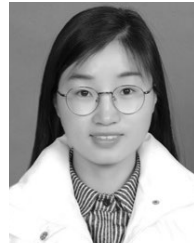
MAO LIU is currently pursuing the master's degree with the School of Electrical and Electronic Engineering, Tianjin University of Technology, Tianjin, China.

His research interests include the grid-connected control of new energy power generation systems and the reliability of high-power wind power converters.

YOUJIE MA received the bachelor's, master's, and Ph.D. degrees in power system and automation from Tsinghua University. From 1993 to 2002, she was with the School of Electrical and Automation Engineering, Qingdao University, and was promoted to full Professor, in 1998. Since 2002, she has been with the School of Automation, Tianjin University of Technology.

SUNA WEN was born in Hebei, China, in 1993. She is currently pursuing the master's degree with the School of Electrical and Electronic Engineering, Tianjin University of Technology, Tianjin, China.

Her research interests include the grid-connected control of new energy power generation systems and treatment scheme microgrid harmonic.

● ● ●